
PHYUNFOLD-NET: ADVANCING REMOTE SENSING CHANGE DETECTION WITH PHYSICS-GUIDED DEEP UNFOLDING

ARXIV PREPRINT

Zelin Lei*
Xi'an Jiaotong University
thedieisnotcast@stu.xjtu.edu.cn

Yaoxing Ren*
Xi'an Jiaotong University
renyaoxing2000@163.com

Jiaming Chang†
Anhui University
jmchang0517@163.com

ABSTRACT

Bi-temporal change detection is highly sensitive to acquisition discrepancies, including illumination, season, and atmosphere, which often cause false alarms. We observe that genuine changes exhibit higher patch-wise singular-value entropy (SVE) than pseudo changes in the feature-difference space. Motivated by this physical prior, we propose PhyUnfold-Net, a physics-guided deep unfolding framework that formulates change detection as an explicit decomposition problem. The proposed Iterative Change Decomposition Module (ICDM) unrolls a multi-step solver to progressively separate mixed discrepancy features into a change component and a nuisance component. To stabilize this process, we introduce a staged Exploration-and-Constraint loss (S-SEC), which encourages component separation in early steps while constraining nuisance magnitude in later steps to avoid degenerate solutions. We further design a Wavelet Spectral Suppression Module (WSSM) to suppress acquisition-induced spectral mismatch before decomposition. Experiments on four benchmarks show improvements over state-of-the-art methods, with gains under challenging conditions.

Keywords Remote sensing · Bi-temporal change detection · Deep unfolding · Singular-value entropy

1 Introduction

Change detection in bi-temporal remote sensing imagery underpins large-scale Earth observation tasks such as urban expansion monitoring, land-use analysis, and disaster assessment in dynamic environments. Deep learning has driven steady progress, from Siamese CNNs [1, 2] to Transformer-based architectures [3–5] that capture long-range context. Nevertheless, robust change detection under complex acquisition conditions remains challenging.

Images captured at different times often vary in illumination, season, and atmospheric conditions in practical acquisition pipelines. These acquisition gaps can introduce pseudo changes and obscure true semantic changes, making direct prediction from raw bi-temporal features unreliable.

However, most existing change detection methods suppress nuisance in an implicit manner, resulting in incomplete filtration. Existing methods primarily employ cross-temporal attention or token interaction with difference enhancement. As shown in Fig. 1(a), cross-temporal attention learns invariant correspondences between I_1 and I_2 to attenuate appearance-induced disturbances before predicting \hat{Y} . Fig. 1(b) illustrates token interaction with difference enhancement, which boosts discriminative discrepancies but still entangles true change with nuisance in learned features. In contrast, as shown in Fig. 1(c), our difference-space formulation $D = \Delta(F_1, F_2)$ explicitly decomposes features into a change component C and a nuisance component N via an unrolled K -step solver, enabling stable and controllable refinement while using C for final prediction.

In this paper, we present **PhyUnfold-Net**, a physics-guided deep unfolding framework that casts bi-temporal change detection as a structured decomposition of the feature-difference map D into a change component C and a nuisance component N . Our method builds on an unrolled K -step solver [6, 7] in which residual-driven updates progressively refine (C, N) . SVE-guided gating, staged regularization, and wavelet-based spectral consistency jointly strengthen the

*Equal contribution.

†Corresponding author.

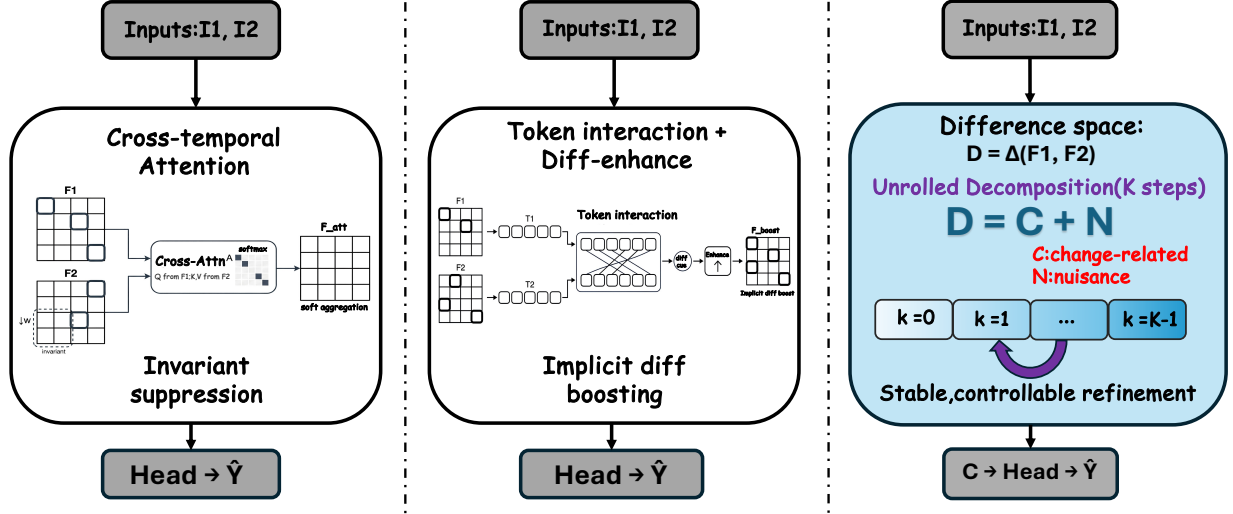


Figure 1: Paradigm comparison. (a) Cross-temporal attention for invariant suppression. (b) Token interaction with implicit difference boosting. (c) Our explicit difference-space decomposition $D = C + N$ with unrolled refinement for stable, controllable change modeling with explicit separation control.

decomposition and suppress acquisition-induced nuisance, yielding a robust and interpretable change-modeling method. Our main contributions are briefly summarized as follows, with emphasis on explicit decomposition, stable unrolled optimization, and spectral-consistency learning:

1. We introduce **PhyUnfold-Net**, a physics-guided deep unfolding framework that formulates bi-temporal change detection as an explicit difference-space decomposition of D into (C, N) with clear physical interpretability.
2. A memory-enhanced unrolled solver, **ICDM**, is designed with SVE-gated residual injection to stabilize refinement in nuisance-dominated regions while preserving fine structures and stable convergence.
3. For training stability, **S-SEC** is developed as a staged regularization scheme that couples margin-based component separation with bounded nuisance-energy constraints, effectively preventing degenerate decompositions.
4. We incorporate **WSSM** to align multi-frequency structures across time via wavelet-based spectral suppression, thereby suppressing acquisition-induced variations and improving robustness.

2 Related Work

Remote Sensing Change Detection. Change detection has evolved from classical image differencing to models that learn discriminative bi-temporal representations. A paradigm is a Siamese encoder [1, 8] followed by fusion operators (concatenation, subtraction, correlation) and a segmentation head [2, 9]. Recent work strengthens this pipeline with multi-scale pyramids [10], context aggregation [11, 12], attention mechanisms [13, 14], lightweight modeling [15], and modern sequence models (Transformers/SSMs) [3–5, 16–18]. Despite benchmark progress, robustness remains a bottleneck: illumination, seasonal shifts, and residual misregistration produce differences that dominate true change cues, and most methods suppress these implicitly through model capacity.

Deep Unfolding Networks. Deep unfolding maps iterative solvers into trainable networks with step-wise refinement [6, 7, 19, 20]. By embedding algorithm-inspired update rules, unrolled architectures provide a principled way to inject priors, control the refinement trajectory, and share parameters across steps. Unrolling has shown clear benefits in inverse problems [6, 7, 20]. However, direct unrolling is not always stable: residual updates may amplify errors when intermediate states are uncertain, and repeated transformations can erode fine structures. Compact recurrent memory [21, 22] offers a principled remedy by preserving useful information across steps under long-horizon refinement.

3 Preliminaries

Notation and Problem Setting. Given a bi-temporal image pair (I_1, I_2) with $I_t \in \mathbb{R}^{H \times W \times c}$ ($t \in \{1, 2\}$), the goal is to predict a binary change mask $Y \in \{0, 1\}^{H \times W}$. A Siamese feature extractor $E(\cdot)$ maps each image to a feature map:

$$F_t = E(I_t) \in \mathbb{R}^{H' \times W' \times d}, \quad t \in \{1, 2\}. \quad (1)$$

After that, a mixed discrepancy feature D is constructed through an operator Δ :

$$D = \Delta(F_1, F_2) \in \mathbb{R}^{H' \times W' \times d}. \quad (2)$$

Instead of predicting directly from D , we reformulate the problem as

$$D = C + N, \quad (3)$$

where C denotes change-related content and N denotes nuisance content.

To regularize this decomposition, we formulate the objective as:

$$\min_{C, N} \underbrace{\mathcal{L}_{\text{rec}}(C, N; D)}_{\text{data fidelity}} + \lambda_C \mathcal{R}_C(C) + \lambda_N \mathcal{R}_N(N), \quad (4)$$

The data-fidelity term is $\mathcal{L}_{\text{rec}}(C, N; D) = \|D - (C + N)\|_1$, while \mathcal{R}_C and \mathcal{R}_N are generic priors weighted by λ_C and λ_N . PhyUnfold-Net unrolls a solver for (4) into K learnable steps (ICDM) to iteratively refine (C, N) .

Unrolled Refinement Operator. Let (C^k, N^k) denote the refinement state at step k . We denote the learned refinement operator by

$$(C^{k+1}, N^{k+1}) = \mathcal{T}_{\theta_k}(C^k, N^k; D), \quad k = 0, \dots, K-1, \quad (5)$$

Here, \mathcal{T}_{θ_k} is parameterized by neural modules, and parameters can be shared across steps. This formulation turns iterative refinement into a learnable operator with step-wise control.

Patch-wise singular-value entropy. We quantify local spectral complexity via patch-wise singular-value entropy (SVE). Given a feature map $X \in \mathbb{R}^{d \times H' \times W'}$, we partition its spatial domain into N non-overlapping square patches of side length p (stride p).

$$\mathcal{P}_j = \{(u, v) \mid u \in [u_j, u_j + p - 1], v \in [v_j, v_j + p - 1]\},$$

and denote the corresponding cropped tensor by $X_{\mathcal{P}_j} \in \mathbb{R}^{d \times p \times p}$. We reshape each patch into a channel-spatial matrix

$$M_j = \text{reshape}(X_{\mathcal{P}_j}) \in \mathbb{R}^{d \times L}, \quad L = p^2, \quad (6)$$

whose columns enumerate the p^2 spatial locations and whose rows correspond to channels. Let the singular values of M_j be $\sigma_j = [\sigma_{j,1}, \dots, \sigma_{j,r_j}]$ with $r_j = \min(d, L)$. We define the normalized spectrum

$$p_{j,i} = \frac{\sigma_{j,i}}{\sum_{\ell=1}^{r_j} \sigma_{j,\ell}}, \quad i = 1, \dots, r_j, \quad (7)$$

and compute the patch-wise SVE

$$s_j = - \sum_{i=1}^{r_j} p_{j,i} \log(p_{j,i} + \epsilon). \quad (8)$$

Finally, we form a dense map $S \in \mathbb{R}^{H' \times W'}$ by assigning s_j to all pixels in its patch region \mathcal{P}_j (i.e., $S(u, v) = s_j$ for $(u, v) \in \mathcal{P}_j$).

4 The Proposed Method

We illustrate the overall pipeline of PhyUnfold-Net in Fig. 2. Given bi-temporal images (I_1, I_2) , a Siamese encoder $E(\cdot)$ extracts feature fields (F_1, F_2) . To mitigate acquisition-induced appearance discrepancies, we first apply WSSM as a wavelet-domain pre-suppression module at stages 2–4. Then, we fuse the cleaned stage-3 and stage-4 features to form the difference map $D = \Delta(\tilde{F}_1, \tilde{F}_2)$. PhyUnfold-Net models D as an explicit decomposition $D = C + N$ and performs K -step unrolled refinement via ICDM; residual-driven updates progressively refine (C, N) under spectral-aware gating and lightweight recurrent memory. The final prediction is produced from the change component C^K by a segmentation head, and training further incorporates reconstruction and staged regularization terms as indicated in the figure.

4.1 Memory-Enhanced ICDM with SVE-Gated Residual Injection

Given a bi-temporal pair (I_1, I_2) , a Siamese encoder $E(\cdot)$ extracts features $F_t = E(I_t)$ for $t \in \{1, 2\}$ and builds the discrepancy field $D = \Delta(F_1, F_2)$. Considering that D contains both genuine change cues and acquisition-induced perturbations, we design an explicit decomposition:

$$D = C + N, \quad (9)$$

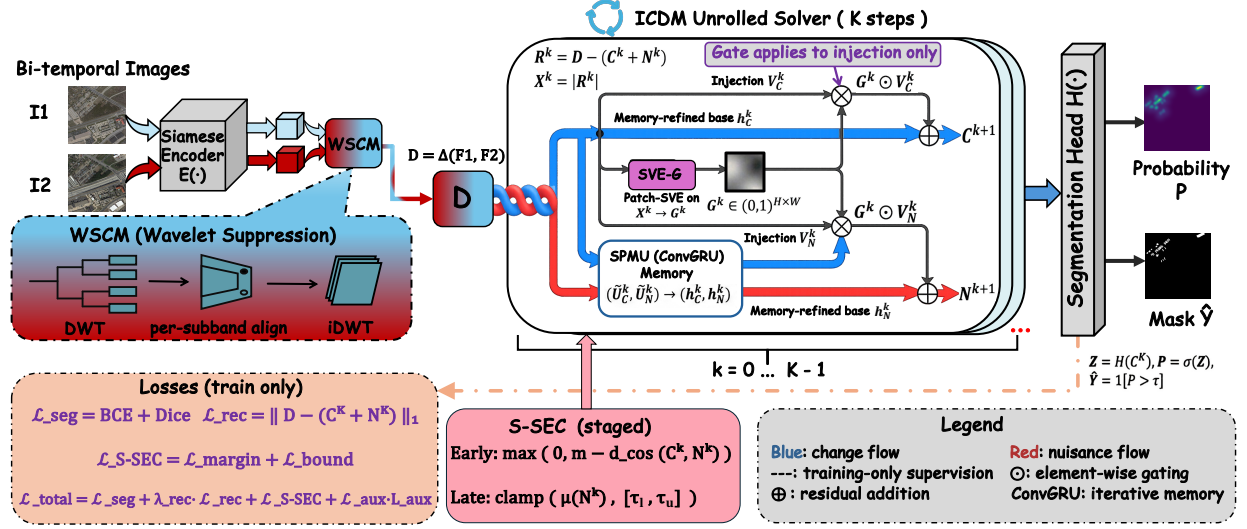


Figure 2: Overview of PhyUnfold-Net. WSCM pre-suppresses acquisition-induced variations before forming $D = \Delta(F_1, F_2)$; ICDM unrolls a K -step solver to decompose $D = C + N$ and refine (C, N) ; the segmentation head predicts \hat{Y} from C^K , with training-time losses and staged regularization shown in the lower panels.

in which C accumulates change-related content and N absorbs nuisance variations in a complementary manner across steps.

This design is motivated by a physical observation that acquisition noise often appears as locally uncertain mismatch patterns. Based on this prior, ICDM designs a K -step unfolding process. Initialization is set to $C^0 = \mathbf{0}$ and $N^0 = D$, so evidence of true change is progressively extracted from a nuisance-dominated starting point during iterative refinement. At iteration k , we first evaluate the decomposition-consistency residual term

$$R_{\text{res}}^k = D - (C^k + N^k), \quad (10)$$

which quantifies the mismatch between the observed difference map and the current reconstruction. Instead of updating the two branches independently, ICDM predicts coupled update directions from their joint context

$$\Delta C^k = \Phi_C([C^k, N^k, R_{\text{res}}^k]), \quad \Delta N^k = \Phi_N([C^k, N^k, R_{\text{res}}^k]), \quad (11)$$

Here, $[\cdot]$ denotes channel concatenation, and Φ_C, Φ_N are lightweight learnable operators. This yields two complementary corrections, including a base update along the predicted directions and a residual reinjection path for unresolved discrepancies in challenging regions:

$$\tilde{U}_C^k = \alpha_k \Delta C^k, \quad \tilde{U}_N^k = \beta_k \Delta N^k, \quad (12)$$

$$V_C^k = \gamma_k \Psi_C(R_{\text{res}}^k), \quad V_N^k = \gamma_k \Psi_N(R_{\text{res}}^k), \quad (13)$$

The learnable scalars $\alpha_k, \beta_k, \gamma_k$ control step amplitudes, and Ψ_C, Ψ_N are 1×1 projections. To prevent long-horizon drift while preserving fine structures, we first form provisional states using only the base increments:

$$\tilde{C}^{k+1} = C^k + \tilde{U}_C^k, \quad \tilde{N}^{k+1} = N^k + \tilde{U}_N^k. \quad (14)$$

We then propagate compact recurrent memories:

$$h_C^k = \text{Mem}_C(\tilde{C}^{k+1}, h_C^{k-1}), \quad h_N^k = \text{Mem}_N(\tilde{N}^{k+1}, h_N^{k-1}), \quad (15)$$

with initialization $h_C^{-1} = h_N^{-1} = 0$. In practice, $\text{Mem}_C, \text{Mem}_N$ are implemented as a **Shared-Parameter Memory Unit (SPMU)** based on lightweight gated recurrent units with convolutional state transitions, following design principles from GRU and ConvLSTM [21, 22], and are shared across steps throughout unrolling for stable and parameter-efficient refinement.

The same physical prior further suggests that nuisance-dominated mismatch is locally uncertain. Accordingly, residual reinjection should be spatially moderated rather than uniformly applied. We derive a local uncertainty signal from residual magnitude at each spatial location,

$$X^k = |R_{\text{res}}^k| \in \mathbb{R}^{d \times H' \times W'}, \quad (16)$$

and reduce channels before entropy estimation:

$$\bar{X}^k = \Pi(X^k) \in \mathbb{R}^{d_{\text{sve}} \times H' \times W'}, \quad d_{\text{sve}} \ll d. \quad (17)$$

Channel reduction is implemented by a learnable 1×1 projection $\Pi(\cdot)$. Patch-wise SVE on \bar{X}^k (Sec. 3) produces an entropy map $S^k \in \mathbb{R}^{H' \times W'}$, which is mapped to a gate for adaptive residual reinjection:

$$G^k = \text{sigmoid}(\phi(S^k)), \quad (18)$$

A lightweight mapper $\phi(\cdot)$ transforms S^k into $G^k \in (0, 1)^{H' \times W'}$. The final update applies this gate only to residual reinjection,

$$C^{k+1} = h_C^k + (G^k \otimes \mathbf{1}) \odot V_C^k, \quad N^{k+1} = h_N^k + (G^k \otimes \mathbf{1}) \odot V_N^k. \quad (19)$$

In Eq. (19), \odot denotes element-wise multiplication, and $G^k \otimes \mathbf{1}$ broadcasts the 2D gate over channels. This gate modulates residual corrections spatially, preventing uniform reinjection in heterogeneous regions. Repeating this refinement for K iterations yields (C^K, N^K) as the final decomposed representation.

Given the final change-related component C^K , a lightweight segmentation head $H(\cdot)$ predicts logits and probabilities as

$$Z = H(C^K), \quad P = \sigma(Z), \quad \hat{Y} = \mathbb{I}[P > \tau], \quad (20)$$

with sigmoid activation $\sigma(\cdot)$ and decision threshold τ ; during training, segmentation supervision is applied to the bilinearly upsampled P (from $H' \times W'$ to $H \times W$), while \hat{Y} is used only for inference.

4.2 Training Objective and Inference

Explicit decomposition may admit trivial solutions ($C=D, N=0$ or $C=0, N=D$) if unconstrained. Therefore, we adopt a staged **Exploration-and-Constraint objective (S-SEC)** that encourages early separation between components and bounds nuisance energy at later steps. The separation measure is defined as:

$$d(C^k, N^k) = 1 - \frac{\langle \text{vec}(C^k), \text{vec}(N^k) \rangle}{\|\text{vec}(C^k)\|_2 \|\text{vec}(N^k)\|_2 + \epsilon}. \quad (21)$$

This metric operates on vectorized features via $\text{vec}(\cdot)$ and inner product $\langle \cdot, \cdot \rangle$; $\epsilon > 0$ avoids division by zero for numerical stability. In early iterations, we enforce a margin-based separation:

$$\mathcal{L}_{\text{exp}} = \sum_{k \in \mathcal{K}_e} \max(0, m - d(C^k, N^k)). \quad (22)$$

The margin is set by m , and \mathcal{K}_e collects early unrolling steps for explicit component exploration. In later iterations, we constrain the mean absolute magnitude of the nuisance term N^k :

$$\mu(N^k) = \frac{1}{H' W' d} \sum_{u=1}^{H'} \sum_{v=1}^{W'} \sum_{c=1}^d |N_c^k(u, v)|. \quad (23)$$

The statistic $\mu(N^k)$ averages absolute nuisance magnitude over all $H' \times W'$ spatial locations and all d channels at each step. We further enforce a bounded range to avoid energy collapse or component swapping:

$$\mathcal{L}_{\text{con}} = \sum_{k \in \mathcal{K}_1} \left[\max(0, \mu(N^k) - \tau_u) + \max(0, \tau_\ell - \mu(N^k)) \right]. \quad (24)$$

Later-step indices are grouped in \mathcal{K}_1 , and τ_ℓ, τ_u define lower and upper nuisance-energy bounds. The full staged regularizer is

$$\mathcal{L}_{\text{S-SEC}} = \lambda_e \mathcal{L}_{\text{exp}} + \lambda_c \mathcal{L}_{\text{con}}. \quad (25)$$

The coefficients λ_e and λ_c control the strengths of exploration and constraint terms across training stages and phases.

The overall objective combines segmentation supervision with decomposition regularization throughout optimization for stable training:

$$\mathcal{L} = \mathcal{L}_{\text{seg}}(\text{Up}(P), Y) + \lambda_{\text{rec}} \|D - (C^K + N^K)\|_1 + \mathcal{L}_{\text{S-SEC}} + \lambda_{\text{aux}} \mathcal{L}_{\text{aux}}. \quad (26)$$

In the final objective, \mathcal{L}_{seg} combines BCE and Dice losses [23] computed from $(\text{Up}(P), Y)$, $\|D - (C^K + N^K)\|_1$ penalizes final-step reconstruction error, and \mathcal{L}_{aux} provides auxiliary deep supervision; $\lambda_{\text{rec}}, \lambda_{\text{aux}}$ set the corresponding weights. At test time, we run the same K ICDM steps to obtain C^K and produce the final mask using Eq. (20).

4.3 WSSM: Wavelet Spectral Suppression Module

Before unrolled decomposition, we pre-suppress acquisition-induced nuisance at the feature level. Illumination and atmospheric variations primarily affect the low-frequency envelope of feature maps, while genuine structural changes manifest across multiple frequency bands. Given encoder features $F_t^{(l)}$ at stage l ($l \in \{2, 3, 4\}$), we apply a single-level 2D discrete wavelet transform (DWT) with Haar wavelets:

$$\{A_t^{(l)}, H_t^{(l)}, V_t^{(l)}, D_t^{(l)}\} = \text{DWT}(F_t^{(l)}), \quad t \in \{1, 2\}, \quad (27)$$

Index t refers to temporal branch and l to encoder stage; A denotes the low-frequency approximation (LL), while H, V, D are horizontal (LH), vertical (HL), and diagonal (HH) detail subbands. For each subband $S \in \{A, H, V, D\}$, we compute branch-wise cross-temporal residuals and suppress them via learnable 1×1 projections:

$$\hat{S}_1^{(l)} = S_1^{(l)} - \eta_S \cdot \Psi_S(S_1^{(l)} - S_2^{(l)}), \quad \hat{S}_2^{(l)} = S_2^{(l)} + \eta_S \cdot \Psi_S(S_1^{(l)} - S_2^{(l)}). \quad (28)$$

After alignment, $\hat{S}_t^{(l)}$ is the corrected subband feature; η_S controls suppression strength, and Ψ_S is a learnable 1×1 projection for subband S . The low-frequency subband A receives stronger suppression (with η_A initialized higher), while detail subbands use milder corrections to preserve structural edges. The aligned subbands are reconstructed via the inverse DWT:

$$\hat{F}_t^{(l)} = \text{IDWT}(\hat{A}_t^{(l)}, \hat{H}_t^{(l)}, \hat{V}_t^{(l)}, \hat{D}_t^{(l)}). \quad (29)$$

This gives $\hat{F}_t^{(l)}$, the reconstructed and nuisance-suppressed feature map at stage l . The cleaned features $\hat{F}_t^{(l)}$ replace $F_t^{(l)}$ before the difference operator Δ . WSSM adds negligible overhead (four 1×1 convs per stage) and is applied at stages 2–4 of the Siamese encoder in all experiments.

5 Experiments

Physical Prior Validation. We first verify whether the proposed physical prior can emerge in a standard backbone without any explicit physics-guided module.

We train a UNet on LEVIR-CD and track the SVE of difference features $D=F_2-F_1$ at four representative layers: the deepest encoder stage (Encoder-4) and three decoder stages (Decoder-1, Decoder-2, and Decoder-3). Features are partitioned into 8×8 spatial patches and grouped by ground-truth labels.

Figure 3 shows a clear trend: changed and unchanged patches are close in Encoder-4 and Decoder-1, then separate in Decoder-2, and diverge most in Decoder-3. The unchanged curve keeps decreasing while the changed curve remains in a higher band, indicating that decoding suppresses nuisance complexity while preserving structurally rich change cues. This behavior supports the physical prior used in our method under progressive decoding refinement.

5.1 Datasets and Evaluation Metrics

LEVIR-CD [13, 14] has 637 pairs. We use the default 445 / 64 / 128 split (train / val / test), yielding 7,120 / 1,024 / 2,048 non-overlapping 256×256 patches.

LEVIR-CD+ [24, 25] has 985 pairs. We follow the official 65% / 35% train/test split (no official validation set).

WHU-CD [26] has no official split. Following common practice [14], we use non-overlapping 256×256 crops with a random 6,096 / 762 / 762 split (train / val / test).

S2Looking [25] has 5,000 pairs and 65,920 annotated change instances. We use the official 70% / 10% / 20% split (3,500 / 500 / 1,000 for train / val / test).

Metrics. We report Precision (Pre.), Recall (Rec.), F1-score (F1), and IoU, with F1 and IoU as primary metrics [14].

5.2 Implementation Details

We use ResNet-18 [27] pretrained on ImageNet [28] as the Siamese encoder. WSSM operates on stages 2–4; ICDM runs $K=3$ unrolling steps on the difference map D constructed from fused stage-3 and stage-4 features. All models are trained for 200 epochs with AdamW [29, 30] ($\beta_1=0.9$, $\beta_2=0.999$, weight decay 10^{-4}), batch size 8, polynomial LR schedule (initial 6×10^{-4} , power 0.9), AMP, and EMA (decay 0.995). Augmentation includes random flips and rotation ($\pm 15^\circ$). The inference threshold is set to $\tau=0.4$. All experiments are run on a single NVIDIA RTX 4090 GPU.

SVE Evolution Across UNet Layers During Training

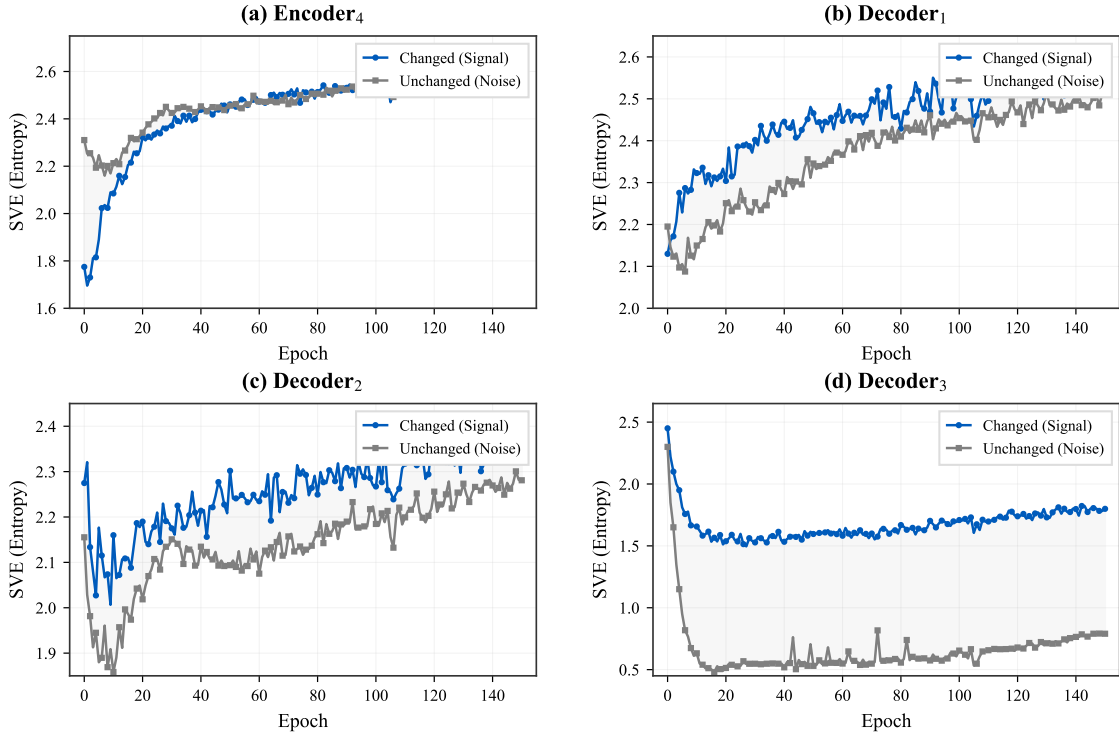


Figure 3: SVE evolution across UNet layers during training, including Encoder-4, Decoder-1, Decoder-2, and Decoder-3 for progressive change-noise separation.

Table 1: Results on LEVIR-CD. Best in **bold**, second-best underlined.

Method	Year	Pre.(%)	Rec.(%)	F1(%)	IoU(%)
FC-Siam-Di [1]	2018	89.53	83.31	86.31	75.92
DTCDCSCN [31]	2021	88.54	86.13	87.32	77.49
STANet [13]	2020	89.06	85.80	87.40	77.67
DSIFN [9]	2020	90.15	87.03	88.56	79.52
SNUNet [2]	2022	89.18	87.17	88.16	78.83
BIT [14]	2022	89.24	89.37	89.31	80.68
RS-Mamba [17]	2024	91.36	88.23	89.77	81.44
ChangeDA [32]	2025	93.67	<u>90.92</u>	<u>92.27</u>	<u>85.65</u>
SPMNet [33]	2025	92.12	90.58	91.34	84.07
PhyUnfold-Net (Ours)	2026	<u>93.41</u>	92.70	93.05	87.00

5.3 Comparison with State-of-the-Art Methods

We compare PhyUnfold-Net with representative CNN-based, attention-based, and Transformer-based methods, including FC-Siam-Di [1], DTCDCSCN [31], DSIFN [9], SNUNet [2], STANet [13], BIT [14], and RS-Mamba [17]. We further include two recent TGRS methods published in 2025, ChangeDA [32] and SPMNet [33], under the same evaluation protocol.

Analysis. Tables 1–4 summarize quantitative comparisons, including two recent 2025 TGRS methods (ChangeDA and SPMNet). RS-Mamba results are reported on all four benchmarks. On LEVIR-CD, PhyUnfold-Net achieves the best Rec./F1/IoU, while ChangeDA provides the highest precision. On LEVIR-CD+, PhyUnfold-Net achieves the best overall scores across all metrics, outperforming both ChangeDA and SPMNet. On WHU-CD, ChangeDA achieves the best Pre./F1/IoU, PhyUnfold-Net obtains the highest recall, and RS-Mamba provides the second-best precision. On S2Looking, ChangeDA achieves the highest precision (72.26%). PhyUnfold-Net achieves the best Rec./F1/IoU (63.28/67.31/50.68), while ChangeDA is second-best on these three metrics. Overall, PhyUnfold-Net demonstrates state-of-the-art performance, achieving the best results on three out of four benchmarks and remaining highly competitive on WHU-CD under the same evaluation protocol.

Table 2: Results on **LEVIR-CD+**. Best in **bold**, second-best underlined.

Method	Year	Pre.(%)	Rec.(%)	F1(%)	IoU(%)
FC-Siam-Di [1]	2018	63.79	55.12	59.14	41.99
DTCDCSCN [31]	2021	66.38	60.51	63.31	46.30
STANet [13]	2020	68.72	57.43	62.58	45.53
DSIFN [9]	2020	71.05	62.87	66.71	50.06
SNUNet [2]	2022	73.91	66.23	69.86	53.69
BIT [14]	2022	73.42	68.89	71.08	55.17
RS-Mamba [17]	2024	79.67	82.19	80.91	67.95
ChangeDA [32]	2025	81.47	79.85	80.65	67.58
SPMNet [33]	2025	<u>83.59</u>	<u>82.60</u>	<u>83.09</u>	<u>71.01</u>
PhyUnfold-Net (Ours)	2026	87.83	83.89	85.82	75.14

Table 3: Results on **WHU-CD**. Best in **bold**, second-best underlined.

Method	Year	Pre.(%)	Rec.(%)	F1(%)	IoU(%)
FC-Siam-Di [1]	2018	47.33	81.53	59.88	42.73
DTCDCSCN [31]	2021	63.92	82.14	71.91	56.15
STANet [13]	2020	79.37	78.52	78.94	65.22
DSIFN [9]	2020	83.40	80.13	81.73	69.10
SNUNet [2]	2022	85.60	87.90	86.73	76.53
BIT [14]	2022	86.64	85.38	86.00	75.44
RS-Mamba [17]	2024	<u>95.50</u>	90.24	92.79	86.55
ChangeDA [32]	2025	96.45	<u>91.91</u>	94.12	88.90
SPMNet [33]	2025	94.67	89.10	91.80	84.84
PhyUnfold-Net (Ours)	2026	93.24	93.48	<u>93.36</u>	<u>87.50</u>

Table 4: Results on **S2Looking**. Best in **bold**, second-best underlined.

Method	Year	Pre.(%)	Rec.(%)	F1(%)	IoU(%)
FC-Siam-Di [1]	2018	38.25	27.64	32.09	19.11
DTCDCSCN [31]	2021	42.16	31.87	36.30	22.17
STANet [13]	2020	43.58	33.25	37.72	23.24
DSIFN [9]	2020	48.33	37.42	42.17	26.72
SNUNet [2]	2022	50.92	40.18	44.91	28.92
BIT [14]	2022	52.74	42.53	47.06	30.79
RS-Mamba [17]	2024	67.18	58.52	62.56	45.52
ChangeDA [32]	2025	72.26	<u>61.45</u>	<u>66.42</u>	49.72
SPMNet [33]	2025	68.92	59.37	63.78	46.85
PhyUnfold-Net (Ours)	2026	<u>71.85</u>	63.28	67.31	50.68

Table 5: Ablation on **S2Looking**. $\Delta F1$ is the gain over baseline (#1).

#	ICDM	WSSM	S-SEC	Pre.(%)	Rec.(%)	F1(%)	IoU(%)	$\Delta F1$
1	X	X	X	53.17	38.62	44.74	28.82	-
2	✓	X	X	57.63	43.78	49.86	33.18	+5.12
3	X	✓	X	59.41	45.32	51.59	34.78	+6.85
4	X	X	✓	55.86	42.17	48.42	31.95	+3.68
5	✓	✓	X	65.28	53.74	57.53	40.37	+12.79
6	✓	X	✓	62.41	50.63	55.91	38.79	+11.17
7	X	✓	✓	61.53	48.97	54.18	37.23	+9.44
8	✓	✓	✓	71.85	63.28	67.31	50.68	+22.57

5.4 Ablation Study

We conduct an ablation study on S2Looking, and all eight variants use the same ResNet-18 encoder and decoder for fair comparison.

Table 5 reveals clear contributions from all three components.

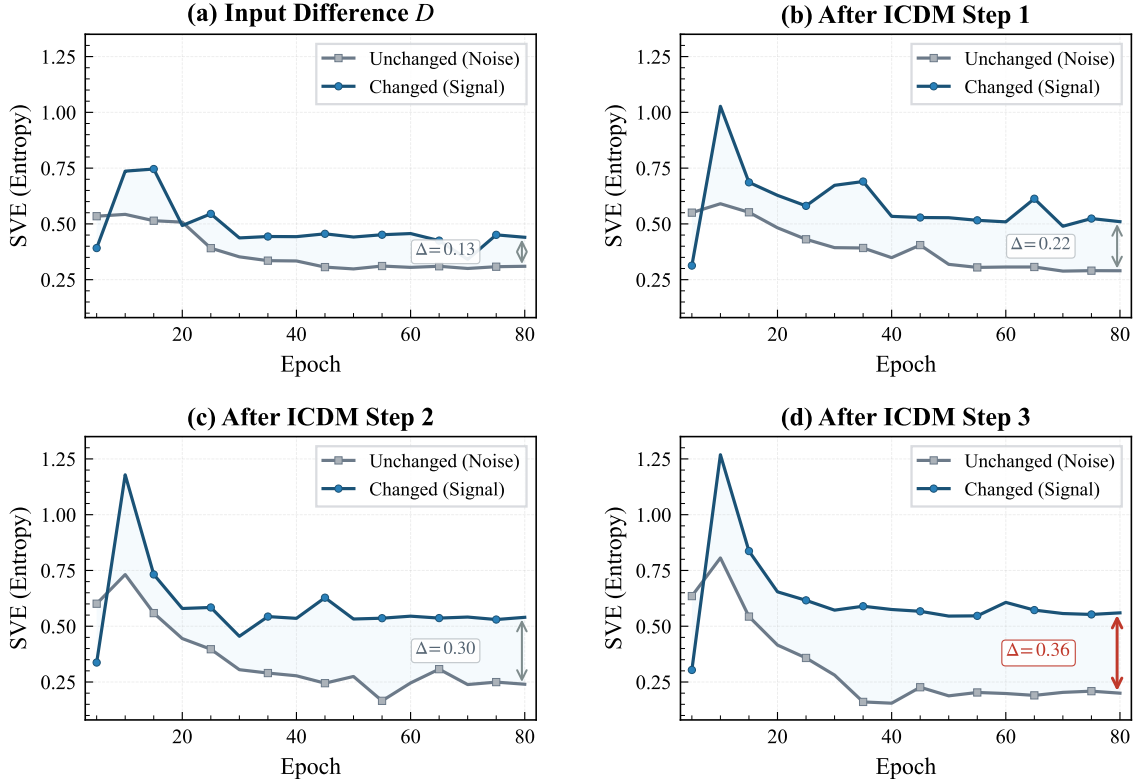


Figure 4: Training-time SVE trajectories for changed and unchanged patches on raw D and ICDM steps $k=1, 2, 3$. The marked end-gap Δ increases from 0.13 to 0.36.

Impact of ICDM. ICDM provides the core decomposition capability. Adding ICDM alone (#2, +5.12%) already improves the baseline (#1) by explicitly establishing the $D = C + N$ separation. When combined with WSSM (#5, +12.79%), the gain is larger than the sum of their standalone improvements, indicating strong complementarity in joint change- nuisance disentanglement.

Effect of WSSM. WSSM is the strongest single module (#3, +6.85%). It also pairs well with ICDM, because cleaner inputs make iterative separation more effective under illumination variation. This synergy suggests that spectral preprocessing and iterative decomposition address complementary sources of nuisance in the change-detection pipeline more thoroughly.

Role of S-SEC. S-SEC acts as a stabilization term. Its standalone gain is moderate (#4, +3.68%). The additional +9.78% gain from #5 to #8 confirms that staged regularization is critical for avoiding degenerate decomposition. The two-phase design (exploration first, then constraint) reflects the intuition that early steps need freedom to separate components before later steps enforce structural compactness and long-term stability.

ICDM step-wise verification. To further validate ICDM, we monitor SVE behavior across unrolling steps during training on LEVIR-CD. Feature maps at each stage are partitioned into 8×8 patches, and SVE is computed per patch grouped by ground-truth labels (changed and unchanged).

To jointly show temporal and spatial evolution, Fig. 4 reports step-wise SVE trajectories and Fig. 5 reports the corresponding patch-grid maps across ICDM steps. We first check whether temporal margin growth is stable across steps and then verify whether the same tendency appears in spatial organization.

Agreement between these two views reduces the chance of interpreting isolated local artifacts as true decoupling. Concretely, valid decoupling should simultaneously show widening margins between changed and unchanged patches in curves and increasingly compact changed-support regions in maps across successive ICDM iterations consistently and reliably.

Effect of unrolling steps K . On LEVIR-CD and LEVIR-CD+, Fig. 6 indicates $K=3$ as the best trade-off: accuracy is near saturation, convergence is faster, and incremental Δ SVE gain beyond $K=3$ is limited while cost keeps increasing. After $K=3$, extra steps mainly increase runtime and memory while bringing marginal gains. The gain from $K=1$

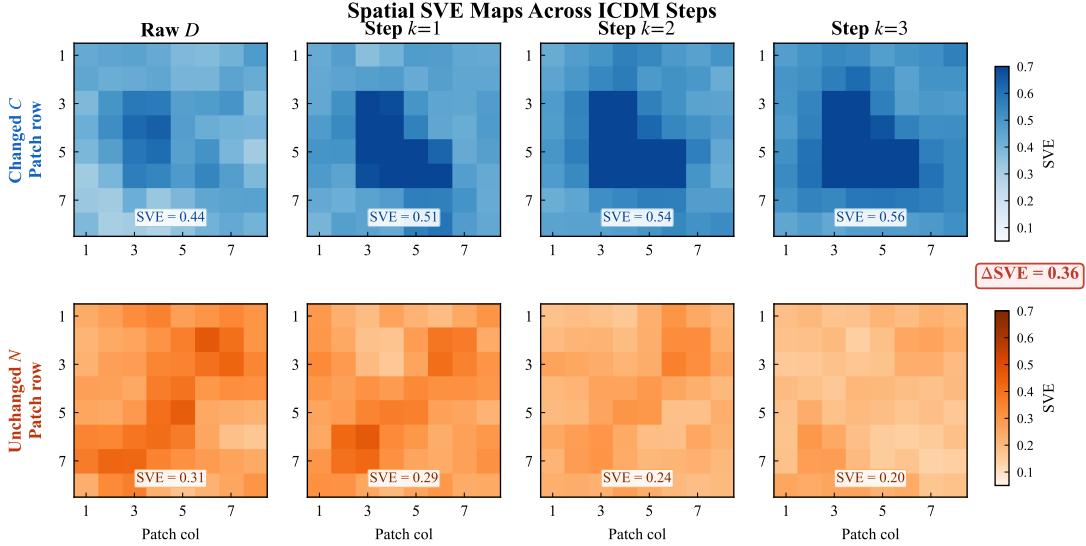


Figure 5: Patch-grid SVE maps across ICDM steps: changed region (top row) becomes progressively more compact and higher-valued, while unchanged region (bottom row) becomes more diffuse and lower-valued over iterative refinement.

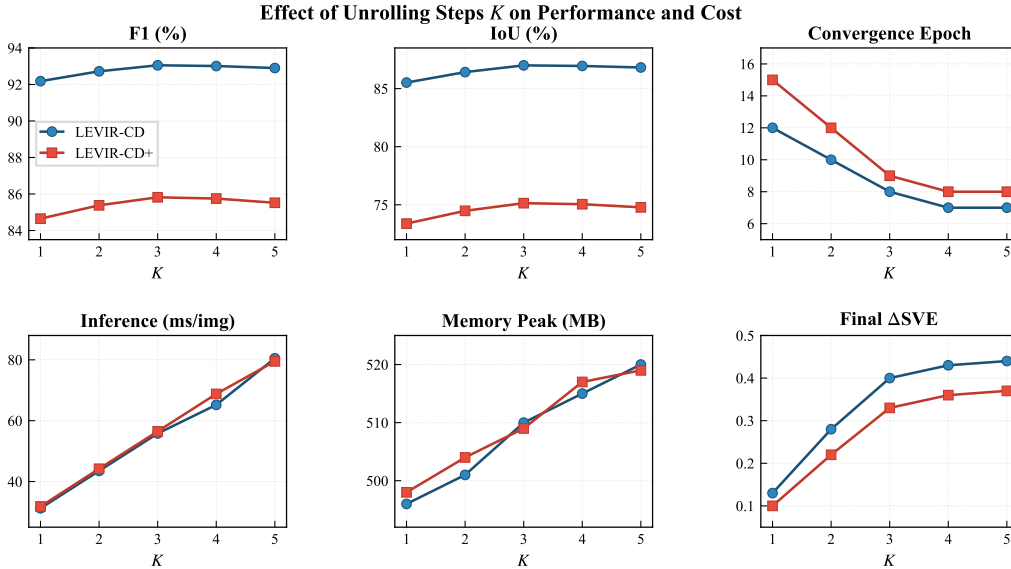


Figure 6: Effect of unrolling steps K on LEVIR-CD and LEVIR-CD+. Dashed lines mark default $K=3$; accuracy saturates while cost grows and ΔSVE gains diminish.

to $K=3$ is larger than from $K=3$ to $K=5$ for similar added runtime and memory, indicating diminishing returns as mismatch is reduced. This motivates the qualitative cross-check in Fig. 7, where we examine whether further unrolling beyond $K=3$ provides substantial structural gains.

Figure 7 visually confirms this trend. At $K=1$, change energy is not fully separated and some structures remain mixed in nuisance responses, whereas at $K=3$ the change component better aligns with true changed regions and gate responses become more selective. At $K=5$, the main changed structures are similar to $K=3$, but extra textures appear, indicating limited structural benefit with slight over-refinement. Together with Fig. 6, this supports choosing $K=3$ as a principled default rather than a tuned heuristic for practical deployment.

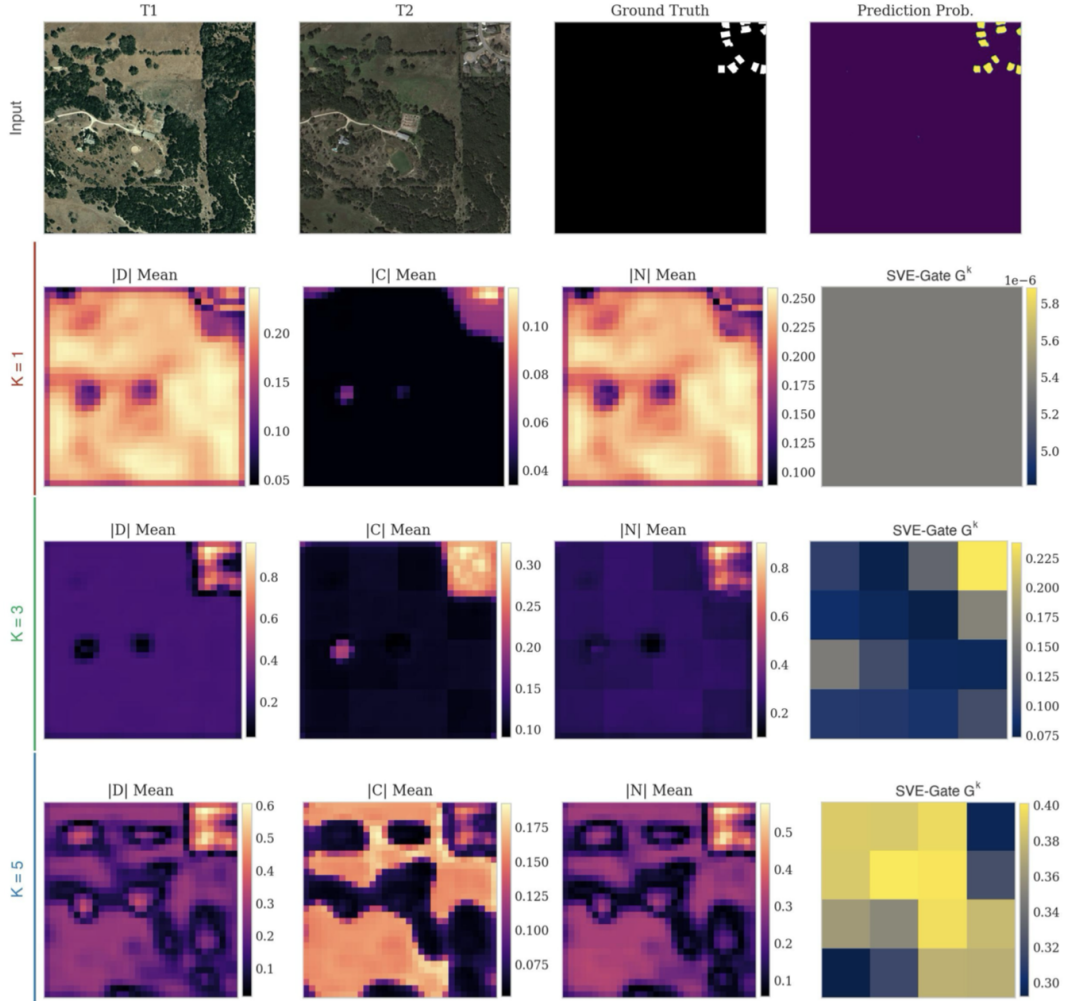


Figure 7: Qualitative decomposition at $K=1, 3, 5$ on LEVIR-CD. $K=1$ is under-decomposed, $K=3$ is clean and discriminative, and $K=5$ brings little gain.

6 Conclusion

In this paper, we present PhyUnfold-Net, a physics-guided deep unfolding framework for bi-temporal change detection via explicit difference-space decomposition. The model integrates ICDM for change- nuisance separation, staged S-SEC regularization for stable decomposition, and WSSM to suppress acquisition-induced spectral mismatch. Experiments on four benchmarks show strong, consistent performance across diverse practical settings, including state-of-the-art results on multiple datasets. Future work will study spatially adaptive entropy estimation and extend to multi-temporal change detection.

This appendix consolidates the additional analyses that were previously prepared as separate supplementary material. Section A presents training dynamics. Section B gives a convergence analysis of ICDM. Section C reports hyperparameter sensitivity for S-SEC.

A Training Dynamics

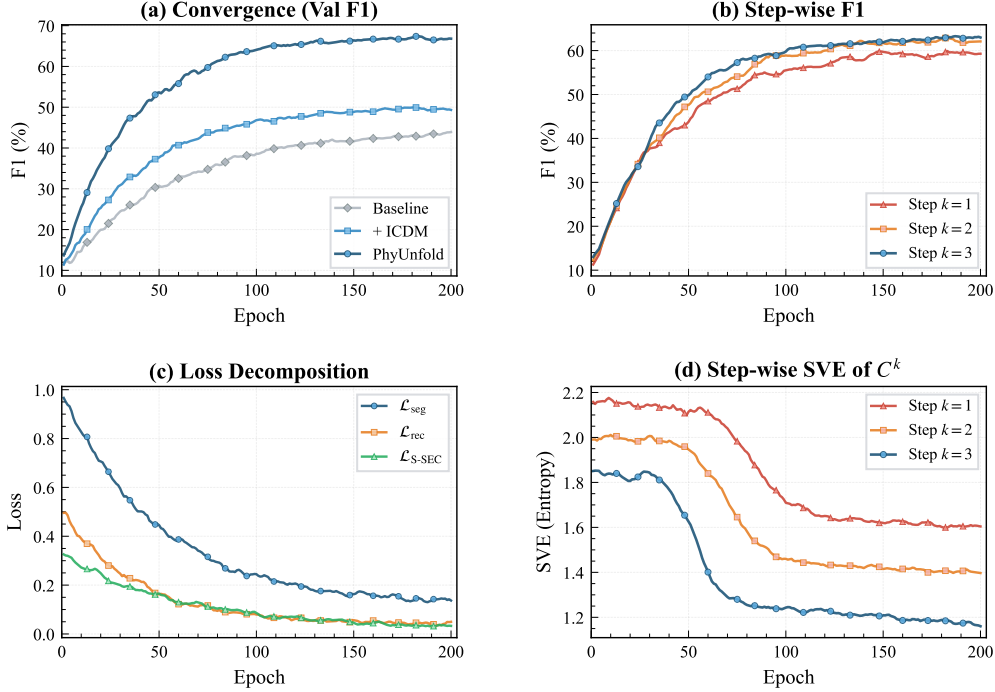


Figure 8: Training dynamics on S2Looking. (a) PhyUnfold-Net converges faster and higher than the baseline and ICDM-only variant. (b) Later ICDM steps consistently yield higher F1. (c) All loss terms decrease smoothly. (d) SVE of C^k shows an overall decreasing trend across steps, confirming progressive spectral concentration.

Figure 8 characterizes the training behavior on S2Looking. **Convergence:** As shown in panel (a), adding ICDM improves both convergence speed and final validation F1 relative to the baseline. The full model (PhyUnfold-Net) converges fastest and reaches the highest plateau among the three settings. **Step-wise F1:** Panel (b) indicates that in the mid-to-late training phase, the step-wise ordering is generally maintained as $k=3 \geq k=2 \geq k=1$. In this phase, the step-1 to step-3 gap is typically about 3–7 percentage points, showing that deeper unrolling provides consistent gains after the early stage. **Loss and SVE:** Panel (c) shows that \mathcal{L}_{seg} , \mathcal{L}_{rec} , and $\mathcal{L}_{\text{S-SEC}}$ follow an overall decreasing trend with minor fluctuations. Panel (d) shows that later steps consistently have lower SVE; and across training, all steps decrease, validating that unrolling progressively concentrates spectral energy.

B Convergence Analysis of ICDM

In the main paper, ICDM unrolls a K -step learnable solver to iteratively refine (C^k, N^k) . This section provides a formal convergence analysis showing a perturbed contractive bound on the decomposition residual and convergence toward the consistency set $\{(C, N) : C + N = D\}$ under mild conditions.

B.1 Formulation Recap

Recall from the ICDM formulation in Sec. 3.1 of the main paper that ICDM initializes $C^0 = \mathbf{0}$, $N^0 = D$, and at each step k computes:

$$R_{\text{res}}^k = D - (C^k + N^k), \quad (30)$$

$$(C^{k+1}, N^{k+1}) = \mathcal{T}_{\theta_k}(C^k, N^k, D), \quad (31)$$

where \mathcal{T}_{θ_k} encapsulates coupled update prediction, base update with learnable step sizes, residual reinjection, provisional update, recurrent memory, and SVE-gated final update at step k .

We analyze convergence through the decomposition residual R_{res}^k , which directly measures how well the current iterate reconstructs D .

B.2 Assumptions

Assumption 1 (Sufficient Contractive Condition). There exists a contraction factor $\rho \in (0, 1)$ such that for all steps $k \geq 1$:

$$\|R_{\text{res}}^{k+1}\|_F \leq \rho \|R_{\text{res}}^k\|_F + \delta_k, \quad (32)$$

where $\delta_k \geq 0$ is a perturbation term arising from SVE gating and memory update, satisfying $\sum_{k=1}^{\infty} \delta_k < \infty$. Note that Eq. (32) does not require monotonic decrease at every step; the initialization transition $k = 0 \rightarrow 1$ is treated as a transient and is not constrained by Eq. (32).

Justification. Assumption 1 is motivated by the architectural design of ICDM: (i) the base update $(\tilde{U}_C^k, \tilde{U}_N^k)$ is explicitly driven by R_{res}^k to reduce reconstruction error; under appropriate step sizes, the reconstruction error is driven by gradient descent and decreases overall across iterations, although local non-monotonic fluctuations may occur due to gating and memory perturbations; (ii) the SVE gate $G^k \in (0, 1)$ suppresses residual reinjection in low-uncertainty regions, limiting perturbation magnitude; (iii) the recurrent memory unit stabilizes updates across steps by smoothing abrupt changes, acting as an implicit regularizer. The perturbation δ_k accounts for the non-ideal gating and memory effects; its summability is supported by the overall decreasing SVE trend observed in Fig. 8(d), which implies that gating corrections diminish as spectral concentration increases. We emphasize that Assumption 1 is a *sufficient condition* for the residual bound; it is not directly verifiable before training and should be interpreted as a structural design rationale rather than a pre-training guarantee.

B.3 Convergence Result

Proposition 1 (Residual Contraction). Under Assumption 1, the decomposition residual satisfies:

$$\|R_{\text{res}}^K\|_F \leq \rho^{K-1} \|R_{\text{res}}^1\|_F + \sum_{j=1}^{K-1} \rho^{K-1-j} \delta_j, \quad K \geq 2. \quad (33)$$

Here, $R_{\text{res}}^k = D - (C^k + N^k)$ denotes the decomposition residual at step k , $K \in \mathbb{N}$ is the total number of iterations, $\rho \in (0, 1)$ is the contraction factor, $\delta_j \geq 0$ is the perturbation term (with $\sum_{j=1}^{\infty} \delta_j < \infty$), and $\|\cdot\|_F$ denotes the Frobenius norm. (For $K=1$ the bound holds trivially as an identity.) As a theoretical reference, if the recursion were extended to $K \rightarrow \infty$ with a shared contraction factor ρ :

$$\limsup_{K \rightarrow \infty} \|R_{\text{res}}^K\|_F \leq \frac{\bar{\delta}}{1 - \rho}, \quad (34)$$

This asymptotic bound is a theoretical extrapolation of the finite-step recursion and serves as motivation rather than a deployment-time guarantee. Our deployed model uses fixed $K=3$ with step-specific parameters $\{\theta_k\}_{k=1}^3$; the operative bound is Eq. (33) evaluated at $K=3$. Here $\bar{\delta} = \sup_{k \geq 1} \delta_k$. In the idealized limit $\delta_k \rightarrow 0$, $\|R_{\text{res}}^K\|_F \rightarrow 0$ and $(C^K + N^K) \rightarrow D$.

Proof. Applying inequality (32) recursively:

$$\begin{aligned} \|R_{\text{res}}^2\|_F &\leq \rho \|R_{\text{res}}^1\|_F + \delta_1, \\ \|R_{\text{res}}^3\|_F &\leq \rho^2 \|R_{\text{res}}^1\|_F + \rho \delta_1 + \delta_2, \\ &\vdots \\ \|R_{\text{res}}^K\|_F &\leq \rho^{K-1} \|R_{\text{res}}^1\|_F + \sum_{j=1}^{K-1} \rho^{K-1-j} \delta_j. \end{aligned} \quad (35)$$

This establishes (33). For the limit, since $\rho < 1$, the first term vanishes as $K \rightarrow \infty$. The second term is bounded by a geometric series: $\sum_{j=1}^{K-1} \rho^{K-1-j} \delta_j \leq \bar{\delta} \sum_{j=0}^{K-2} \rho^j < \frac{\bar{\delta}}{1-\rho}$, yielding (34). When $\delta_k \rightarrow 0$, summability and $\rho < 1$ imply $\|R_{\text{res}}^K\|_F \rightarrow 0$, so $(C^K + N^K) \rightarrow D$. \square

We equip the product space $\mathbb{R}^{d \times H' \times W'} \times \mathbb{R}^{d \times H' \times W'}$ with the standard Euclidean norm $\|(A, B)\|^2 = \|A\|_F^2 + \|B\|_F^2$, and define $\text{dist}(z, \mathcal{M}) = \inf_{z' \in \mathcal{M}} \|z - z'\|$.

Corollary 1 (Consistency-Set Convergence). Define $z^k = (C^k, N^k)$ and

$$\mathcal{M} = \{(C, N) : C + N = D\}.$$

Under Assumption 1:

$$\text{dist}(z^K, \mathcal{M}) = \frac{1}{\sqrt{2}} \|R_{\text{res}}^K\|_F. \quad (36)$$

Consequently,

$$\limsup_{K \rightarrow \infty} \text{dist}(z^K, \mathcal{M}) \leq \frac{\bar{\delta}}{\sqrt{2}(1 - \rho)}, \quad (37)$$

and if $\delta_k \rightarrow 0$, then $\text{dist}(z^K, \mathcal{M}) \rightarrow 0$.

Proof sketch. Let $R = D - (C + N)$ for any pair (C, N) . For feasible corrections $(\Delta C, \Delta N)$ satisfying $\Delta C + \Delta N = R$, the distance to \mathcal{M} is obtained by minimizing $\|\Delta C\|_F^2 + \|\Delta N\|_F^2$. The minimizer is $\Delta C = \Delta N = R/2$, which gives the minimum value $\|R\|_F^2/2$. Applying this identity to (C^K, N^K) yields (36), and (37) follows from Proposition B.3. \square

Remark 1 (Practical implications). Proposition 1 (Residual Contraction) provides a theoretical justification for the choice of K : K only needs to be large enough so that $\rho^{K-1} \|R_{\text{res}}^1\|_F$ is negligible and the residual approaches its perturbation floor. This is consistent with the main-paper K -ablation result: $K=3$ reaches near-saturation performance, while $K>3$ yields diminishing returns.

Remark 2 (Role of SVE gating). The gate G^k is important for reducing the accumulation of $\{\delta_k\}$. Without gating, residual reinjection would apply uniform corrections across all spatial locations, potentially amplifying noise in already-converged regions. The SVE-based gate restricts corrections to high-uncertainty patches, ensuring that perturbation energy diminishes as the decomposition stabilizes.

B.4 Empirical Verification

To empirically examine the contractive trend implied by Proposition 1 (Residual Contraction), we report normalized mismatch scores on the LEVIR-CD and S2Looking test sets after training convergence across ICDM iterations. For ICDM step k , define the normalized mismatch score (the scale-invariant counterpart of the decomposition residual):

$$r^k = \|R_{\text{res}}^k\|_F / \|D\|_F, \quad R_{\text{res}}^k = D - (C^k + N^k).$$

ICDM uses the initialization $C^0 = \mathbf{0}, N^0 = D$, which gives the trivial residual $r^0 = 0$. Therefore, we report non-trivial iteration states $k \in \{1, 2, 3\}$. Note that the increase from $r^0=0$ to $r^1>0$ is expected: the initial assignment $(C^0, N^0)=(\mathbf{0}, D)$ satisfies $C+N=D$ trivially without meaningful separation; the first ICDM step introduces structured decomposition at the cost of a transient reconstruction mismatch, after which the contractive trend takes effect.

Table 6: Normalized mismatch score $r^k = \|R_{\text{res}}^k\|_F / \|D\|_F$ at ICDM steps $k \in \{1, 2, 3\}$. ‘‘Ratio’’ reports r^k / r^{k-1} for $k \geq 2$.

Stage	LEVIR-CD		S2Looking	
	Score r^k	Ratio	Score r^k	Ratio
ICDM $k = 1$	0.412	–	0.487	–
ICDM $k = 2$	0.173	0.420	0.226	0.464
ICDM $k = 3$	0.068	0.393	0.104	0.460

Table 6 shows a clear decrease of r^k across ICDM stages. Within ICDM iterations (from $k = 1 \rightarrow 2$ and $k = 2 \rightarrow 3$), the ratios are approximately stable: 0.420/0.393 on LEVIR-CD and 0.464/0.460 on S2Looking. This trend is consistent with the perturbed contractive behavior assumed in Assumption 1 for non-trivial iterations ($k \geq 1$). The near-constant ratios further suggest that the perturbation terms δ_k are small relative to $\rho \|R_{\text{res}}^k\|_F$, consistent with the summability requirement in Assumption 1. From the first to the third ICDM step, the mismatch score decreases by 83.5% on LEVIR-CD and 78.6% on S2Looking, supporting why $K=3$ is sufficient in practice.

C Hyperparameter Sensitivity of S-SEC

S-SEC introduces five key hyperparameters: margin m , nuisance energy bounds (τ_ℓ, τ_u) , and loss weights (λ_e, λ_c) . We conduct a targeted sensitivity analysis on S2Looking by sweeping one scalar parameter (m) and two coupled parameter pairs $((\tau_\ell, \tau_u), (\lambda_e, \lambda_c))$ around their default settings. Since each pair is swept jointly, individual effects of τ_ℓ vs. τ_u (and λ_e vs. λ_c) are not fully disentangled.

C.1 Separation Margin m

The margin m in \mathcal{L}_{exp} controls the minimum cosine-based separation enforced between C^k and N^k at early steps.

Table 7: Sensitivity to separation margin m on S2Looking. Default: $m=0.3$.

m	Pre.(%)	Rec.(%)	F1(%)	IoU(%)
0.1	67.83	61.42	64.48	47.54
0.2	70.29	62.85	66.37	49.66
0.3	71.85	63.28	67.31	50.68
0.4	71.56	61.93	66.41	49.70
0.5	69.14	60.78	64.71	47.83

Table 7 shows that too small a margin ($m=0.1$) provides insufficient separation pressure, leading to entangled components; too large ($m=0.5$) over-constrains the representation space and degrades recall. Performance peaks at $m=0.3$ with graceful degradation in the range $[0.2, 0.4]$, indicating moderate sensitivity.

C.2 Nuisance Energy Bounds (τ_ℓ, τ_u)

The lower and upper bounds (τ_ℓ, τ_u) in \mathcal{L}_{con} prevent energy collapse ($N \rightarrow 0$) and component swapping at later steps.

Table 8: Sensitivity to nuisance bounds (τ_ℓ, τ_u) on S2Looking. Default: $(0.05, 0.40)$.

τ_ℓ	τ_u	Pre.(%)	Rec.(%)	F1(%)	IoU(%)
0.01	0.20	68.97	60.35	64.38	47.45
0.03	0.30	70.18	62.54	66.15	49.42
0.05	0.40	71.85	63.28	67.31	50.68
0.08	0.50	71.39	62.17	66.48	49.77
0.10	0.60	69.82	61.89	65.63	48.84

A tight bound pair ($\tau_\ell=0.01, \tau_u=0.20$) forces premature nuisance collapse, losing reconstruction fidelity. A loose pair ($\tau_\ell=0.10, \tau_u=0.60$) weakens the constraint and allows excessive energy in N , reintroducing nuisance contamination into C . The default $(0.05, 0.40)$ achieves the best trade-off.

C.3 Loss Weights (λ_e, λ_c)

The exploration weight λ_e and constraint weight λ_c balance \mathcal{L}_{exp} and \mathcal{L}_{con} relative to the primary segmentation loss.

Table 9: Sensitivity to loss weights (λ_e, λ_c) on S2Looking. Default: $(0.5, 1.0)$.

λ_e	λ_c	Pre.(%)	Rec.(%)	F1(%)	IoU(%)
0.1	0.5	68.93	61.07	64.77	47.88
0.3	0.5	70.46	62.73	66.38	49.67
0.5	1.0	71.85	63.28	67.31	50.68
0.5	2.0	71.68	62.41	66.73	50.05
1.0	1.0	70.51	62.19	66.11	49.39
1.0	2.0	69.37	60.54	64.66	47.76

When both weights are small ($\lambda_e = 0.1, \lambda_c = 0.5$), S-SEC provides weak regularization and decomposition quality degrades. Overly strong regularization ($\lambda_e = 1.0, \lambda_c = 2.0$) competes with \mathcal{L}_{seg} and harms segmentation accuracy. A moderate setting, such as $\lambda_e = 0.5$ and $\lambda_c = 1.0$, yields the best performance. Notably, increasing λ_c from 1.0 to 2.0 at fixed $\lambda_e = 0.5$ causes a limited 0.58-point F1 drop ($67.31 \rightarrow 66.73$), suggesting that the boundedness constraint is naturally well-scaled.

C.4 Summary

Across all tested settings, F1 remains within 2.93 points of the default setting (67.31), confirming that PhyUnfold-Net is moderately robust to hyperparameter choices. The largest observed drop appears in the nuisance-bound sweep (67.31→64.38), with the margin sweep close behind (67.31→64.48). The loss-weight sweep shows a comparatively broader stable region, consistent with its role as soft regularization rather than a hard structural constraint.

References

- [1] Rodrigo Caye Daudt, Bertr Le Saux, and Alexandre Boulch. Fully convolutional siamese networks for change detection. In *Proceedings of the IEEE International Conference on Image Processing (ICIP)*, pages 4063–4067, 2018. doi:10.1109/ICIP.2018.8451652.
- [2] Sheng Fang, Kaiyu Li, Jinyuan Shao, and Zhe Li. Snunet-cd: A densely connected siamese network for change detection of vhr images. *IEEE Geoscience and Remote Sensing Letters*, 19:1–5, 2022. doi:10.1109/LGRS.2021.3056416.
- [3] Ashish Vaswani, Noam Shazeer, Niki Parmar, Jakob Uszkoreit, Llion Jones, Aidan N. Gomez, Lukasz Kaiser, and Illia Polosukhin. Attention is all you need. In *Advances in Neural Information Processing Systems (NeurIPS)*, volume 30, pages 5998–6008, 2017.
- [4] Alexey Dosovitskiy, Lucas Beyer, Alexander Kolesnikov, Dirk Weissenborn, Xiaohua Zhai, Thomas Unterthiner, Mostafa Dehghani, Matthias Minderer, Georg Heigold, Sylvain Gelly, Jakob Uszkoreit, and Neil Houlsby. An image is worth 16x16 words: Transformers for image recognition at scale. In *International Conference on Learning Representations (ICLR)*, 2021.
- [5] Ze Liu, Yutong Lin, Yue Cao, Han Hu, Yixuan Wei, Zheng Zhang, Stephen Lin, and Baining Guo. Swin transformer: Hierarchical vision transformer using shifted windows. In *Proceedings of the IEEE/CVF International Conference on Computer Vision (ICCV)*, pages 9992–10002, 2021. doi:10.1109/ICCV48922.2021.00986.
- [6] Karol Gregor and Yann LeCun. Learning fast approximations of sparse coding. In *Proceedings of the 27th International Conference on Machine Learning (ICML)*, pages 399–406, 2010.
- [7] Vishal Monga, Yuelong Li, and Yonina C. Eldar. Algorithm unrolling: Interpretable, efficient deep learning for signal and image processing. *IEEE Signal Processing Magazine*, 38(2):18–44, 2021. doi:10.1109/MSP.2020.3016905.
- [8] Olaf Ronneberger, Philipp Fischer, and Thomas Brox. U-net: Convolutional networks for biomedical image segmentation. In *Medical Image Computing and Computer-Assisted Intervention (MICCAI)*, pages 234–241, 2015. doi:10.1007/978-3-319-24574-4_28.
- [9] Chenxiao Zhang, Peng Yue, Deodato Tapete, Liangcun Jiang, Boyi Shangguan, Li Huang, and Guangchao Liu. A deeply supervised image fusion network for change detection in high resolution bi-temporal remote sensing images. *ISPRS Journal of Photogrammetry and Remote Sensing*, 166:183–200, 2020. doi:10.1016/j.isprsjprs.2020.06.003.
- [10] Tsung-Yi Lin, Piotr Dollar, Ross Girshick, Kaiming He, Bharath Hariharan, and Serge Belongie. Feature pyramid networks for object detection. In *Proceedings of the IEEE Conference on Computer Vision and Pattern Recognition (CVPR)*, pages 936–944, 2017. doi:10.1109/CVPR.2017.106.
- [11] Chengxi Han, Chen Wu, Haonan Guo, Meiqi Hu, and Hongruixuan Chen. Hanet: A hierarchical attention network for change detection with bitemporal very-high-resolution remote sensing images. *IEEE Journal of Selected Topics in Applied Earth Observations and Remote Sensing*, 16:3867–3878, 2023. doi:10.1109/JSTARS.2023.3264802.
- [12] Chao-Peng Chen, Jun-Wei Wu, Lyu-Guang Chen, and Wei Wan. Saras-net: Scale and relation aware siamese network for change detection. In *Proceedings of the AAAI Conference on Artificial Intelligence*, volume 37, pages 14187–14195, 2023. doi:10.1609/aaai.v37i12.26660.
- [13] Hao Chen and Zhenwei Shi. A spatial-temporal attention-based method and a new dataset for remote sensing image change detection. *Remote Sensing*, 12(10):1662, 2020. doi:10.3390/rs12101662.
- [14] Hao Chen, Zipeng Qi, and Zhenwei Shi. Remote sensing image change detection with transformers. *IEEE Transactions on Geoscience and Remote Sensing*, 60:1–14, 2022. doi:10.1109/TGRS.2021.3095166.
- [15] Andrea Codegoni, Gabriele Lombardi, and Alessandro Ferrari. Tinycd: A (not so) deep learning model for change detection. *Neural Computing and Applications*, 35:8471–8486, 2023. doi:10.1007/s00521-022-08122-3.
- [16] Enze Xie, Wenhai Wang, Zhiding Yu, Anima Anandkumar, Jose M. Alvarez, and Ping Luo. Segformer: Simple and efficient design for semantic segmentation with transformers. In *Advances in Neural Information Processing Systems (NeurIPS)*, volume 34, pages 12077–12090, 2021.
- [17] Sijie Zhao, Hao Chen, Xueliang Zhang, Pengfeng Xiao, Lei Bai, and Wanli Ouyang. Rs-mamba for large remote sensing image dense prediction. *IEEE Transactions on Geoscience and Remote Sensing*, 62:1–14, 2024. doi:10.1109/TGRS.2024.3425540.
- [18] Lei Ding, Haitao Guo, Sicong Liu, Lichao Mou, Jing Zhang, and Lorenzo Bruzzone. Joint spatio-temporal modeling for semantic change detection in remote sensing images. *IEEE Transactions on Geoscience and Remote Sensing*, 62:1–14, 2024. doi:10.1109/TGRS.2024.3362795.
- [19] Amir Beck and Marc Teboulle. A fast iterative shrinkage-thresholding algorithm for linear inverse problems. *SIAM Journal on Imaging Sciences*, 2(1):183–202, 2009. doi:10.1137/080716542.

- [20] Jian Zhang and Bernard Ghanem. Ista-net: Interpretable optimization-inspired deep network for image compressive sensing. In *Proceedings of the IEEE Conference on Computer Vision and Pattern Recognition (CVPR)*, pages 1828–1837, 2018. doi:10.1109/CVPR.2018.00196.
- [21] Kyunghyun Cho, Bart van Merriënboer, Caglar Gulcehre, Dzmitry Bahdanau, Fethi Bougares, Holger Schwenk, and Yoshua Bengio. Learning phrase representations using rnn encoder-decoder for statistical machine translation. In *Proceedings of the 2014 Conference on Empirical Methods in Natural Language Processing (EMNLP)*, pages 1724–1734, 2014. doi:10.3115/v1/D14-1179.
- [22] Xingjian Shi, Zhourong Chen, Hao Wang, Dit-Yan Yeung, Wai-Kin Wong, and Wang-Chun Woo. Convolutional lstm network: A machine learning approach for precipitation nowcasting. In *Advances in Neural Information Processing Systems (NeurIPS)*, volume 28, pages 802–810, 2015.
- [23] Fausto Milletari, Nassir Navab, and Seyed-Ahmad Ahmadi. V-net: Fully convolutional neural networks for volumetric medical image segmentation. In *Proceedings of the International Conference on 3D Vision (3DV)*, pages 565–571, 2016. doi:10.1109/3DV.2016.79.
- [24] Qian Shi, Mengxi Liu, Shengchen Li, Xiaoping Liu, Fei Wang, and Liangpei Zhang. A deeply supervised attention metric-based network and an open aerial image dataset for remote sensing change detection. *IEEE Transactions on Geoscience and Remote Sensing*, 60:1–16, 2022. doi:10.1109/TGRS.2021.3085870.
- [25] Li Shen, Yao Lu, Hao Chen, Hao Wei, Donghai Xie, Jiabao Yue, Rui Chen, Shouye Lv, and Bitao Jiang. S2looking: A satellite side-looking dataset for building change detection. *Remote Sensing*, 13(24):5094, 2021. doi:10.3390/rs13245094.
- [26] Shunping Ji, Shiqing Wei, and Meng Lu. Fully convolutional networks for multisource building extraction from an open aerial and satellite imagery data set. *IEEE Transactions on Geoscience and Remote Sensing*, 57(1):574–586, 2019. doi:10.1109/TGRS.2018.2858817.
- [27] Kaiming He, Xiangyu Zhang, Shaoqing Ren, and Jian Sun. Deep residual learning for image recognition. In *Proceedings of the IEEE Conference on Computer Vision and Pattern Recognition (CVPR)*, pages 770–778, 2016. doi:10.1109/CVPR.2016.90.
- [28] Jia Deng, Wei Dong, Richard Socher, Li-Jia Li, Kai Li, and Li Fei-Fei. Imagenet: A large-scale hierarchical image database. In *Proceedings of the IEEE Conference on Computer Vision and Pattern Recognition (CVPR)*, pages 248–255, 2009. doi:10.1109/CVPR.2009.5206848.
- [29] Ilya Loshchilov and Frank Hutter. Decoupled weight decay regularization. *International Conference on Learning Representations (ICLR)*, 2019.
- [30] Diederik P. Kingma and Jimmy Ba. Adam: A method for stochastic optimization. In *International Conference on Learning Representations (ICLR)*, 2015.
- [31] Yi Liu, Chao Pang, Zongqian Zhan, Xiaomeng Zhang, and Xue Yang. Building change detection for remote sensing images using a dual-task constrained deep siamese convolutional network model. *IEEE Geoscience and Remote Sensing Letters*, 18(5):811–815, 2021. doi:10.1109/LGRS.2020.2988032.
- [32] Jiangtao Meng, Xinying Xu, Zhe Zhang, Pengyue Li, Gang Xie, Jinchang Ren, and Yuxuan Zheng. Changeda: Depth-augmented multitask network for remote sensing change detection via differential analysis. *IEEE Transactions on Geoscience and Remote Sensing*, 63:1–19, 2025. doi:10.1109/TGRS.2025.3532468.
- [33] Jiashu Wang, Jinze Song, Hao Zhang, Zekai Zhang, Yunlong Ji, Wenyin Zhang, Jinglin Zhang, and Xing Wang. Spmnet: A siamese pyramid mamba network for very-high-resolution remote sensing change detection. *IEEE Transactions on Geoscience and Remote Sensing*, 63:1–14, 2025. doi:10.1109/TGRS.2025.3565801.